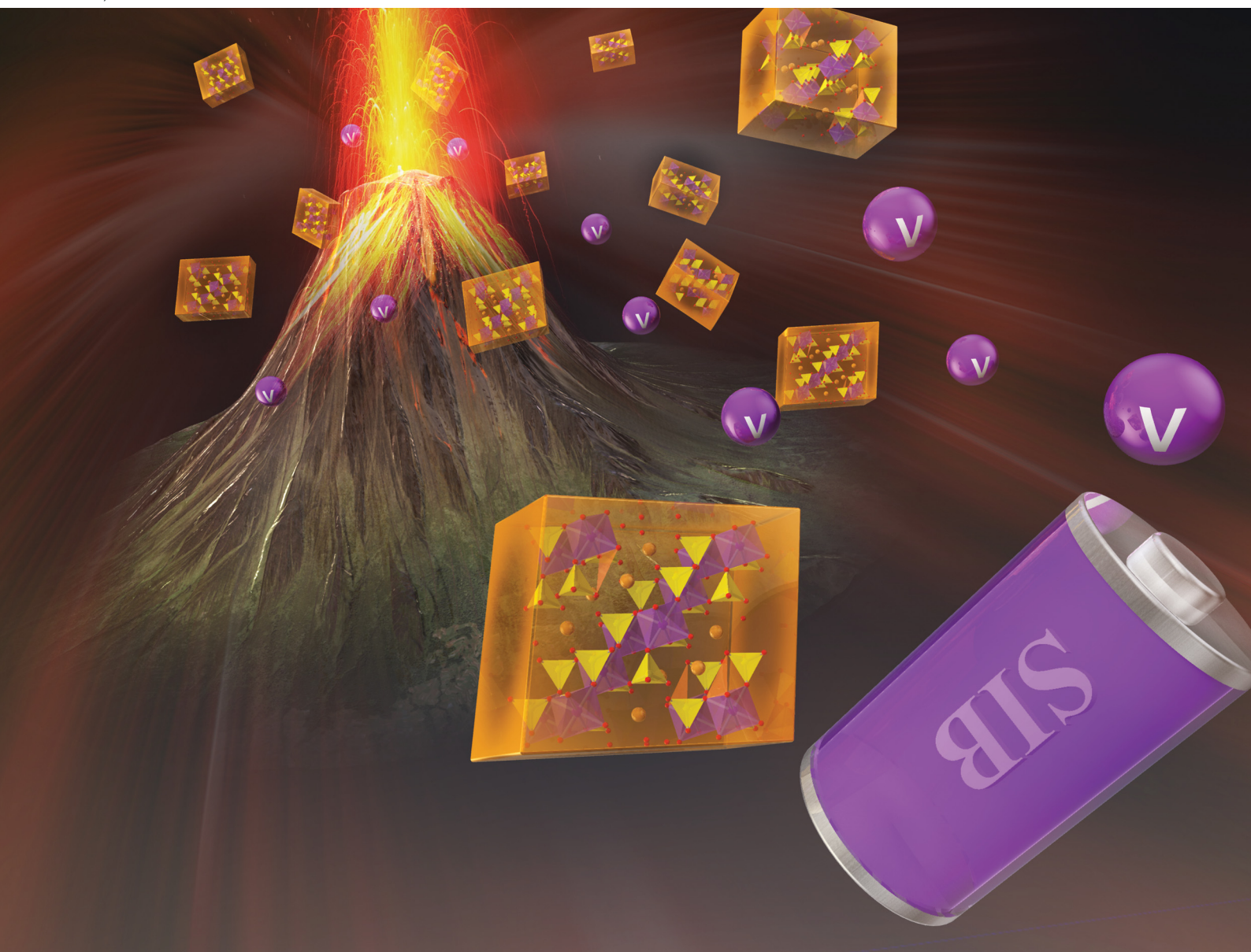


# Materials Advances

Volume 3  
Number 18  
21 September 2022  
Pages 6911–7144

[rsc.li/materials-advances](https://rsc.li/materials-advances)



ISSN 2633-5409

**PAPER**

Akira Nishio, Atsushi Inoishi *et al.*  
Eldfellite-type cathode material,  $\text{NaV}(\text{SO}_4)_2$ ,  
for Na-ion batteries

## PAPER

View Article Online  
View Journal | View IssueCite this: *Mater. Adv.*, 2022,  
3, 6993Received 11th January 2022,  
Accepted 29th June 2022

DOI: 10.1039/d2ma00031h

rsc.li/materials-advances

Eldfellite-type cathode material,  $\text{NaV}(\text{SO}_4)_2$ , for  
Na-ion batteries†Akira Nishio,<sup>a</sup> Yuji Ishado,<sup>b</sup> Kosuke Nakamoto,<sup>b</sup> Eiichi Kobayashi,<sup>c</sup>  
Atsushi Inoishi,<sup>b</sup> Hikari Sakaeb<sup>b</sup> and Shigeto Okada<sup>b</sup>

In this research, an eldfellite-type material containing V as a transition metal,  $\text{NaV}(\text{SO}_4)_2$ , was investigated to achieve higher potentials and capacities through the use of a multi-redox pair. Average working potentials of 3.9 and 2.1 V vs.  $\text{Na}/\text{Na}^+$  were observed, and a large reversible capacity of 102 mA h g<sup>-1</sup> was obtained over a wide potential range. Moreover, X-ray absorption near-edge structure and near-edge X-ray absorption fine structure measurements revealed that only V contributes to the charge compensation in the sodiation/desodiation process at low potentials, whereas both V and O contribute to the desodiation/sodiation process at high potentials. This phenomenon was also supported by the density of states and Bader charge analysis based on the DFT calculations.

## Introduction

With the spread of renewable energy, the demand for large storage batteries as buffers is increasing. For this need, minor metal free Na-ion batteries are attractive as rechargeable batteries with excellent cost performance. However, since the ionic volume of Na is twice that of Li, the  $\text{Na}^+$  diffusivity in the electrodes of Na-ion batteries is less favorable than that of Li-ion batteries. In addition, because the standard electrode potential of Na (−2.71 V vs. standard hydrogen electrode (SHE)) is ~0.3 V higher than that of Li (−3.04 V vs. SHE), the working voltage of a sodium-ion battery is lower than that of a lithium-ion battery.

To overcome these defects, polyanionic materials have been investigated as promising cathode active material groups for Na-ion batteries that fulfil the two requirements of the corner-sharing framework with a large bottleneck for  $\text{Na}^+$  diffusion and an increase of the redox potential through an inductive effect.<sup>1–4</sup> The corner-sharing structures of  $\text{MO}_6$  (M is a 3d transition metal) octahedra and  $\text{XO}_4$  (X is a heteroelement such as Si, P, S, As, Mo, W, etc.) tetrahedra such as NASICON-type  $\text{Na}_x\text{M}_2(\text{XO}_4)_3$  form a suitable bottleneck for the three-dimensional diffusion of  $\text{Na}^+$  ions. Among these heteroelements, polyanions with highly electro-negative heteroelements such as sulfur have an

inductive effect on the electrode potential due to their strong electronic attraction.<sup>5–8</sup>

So far, the following sulfates with a  $\text{Fe}^{2+}/\text{Fe}^{3+}$  redox couple have been reported as cathode active materials for Na-ion batteries:  $\text{Na}_2\text{Fe}_2(\text{SO}_4)_3$  (3.8 V vs.  $\text{Na}/\text{Na}^+$ ),<sup>9</sup>  $\text{Na}_2\text{Fe}(\text{SO}_4)_2$  (3.6 V),<sup>10</sup>  $\text{NaFeSO}_4\text{F}$  (3.5 V),<sup>11,12</sup>  $\text{NaFe}(\text{SO}_4)_2$  (3.3 V),<sup>13</sup>  $\text{Na}_2\text{Fe}(\text{SO}_4)_2 \cdot 2\text{H}_2\text{O}$  (3.25 V),<sup>14</sup>  $\text{Fe}_2(\text{SO}_4)_3$  (3.2 V),<sup>15,16</sup> and  $\text{NaF-FeSO}_4$  (3.0 V).<sup>17</sup> Although there are some variations in the potential, it is noteworthy that sulfates show a higher potential of about 1 V than phosphates such as  $\text{Na}_3\text{Fe}_2(\text{PO}_4)_3$  (2.5 V).<sup>18–20</sup> On the other hand, the disadvantage of the polyanionic cathode is that the theoretical capacity is limited by the heavy molecular weight. In particular, eldfellite-type  $\text{NaFe}(\text{SO}_4)_2$  (theoretical capacity: 99 mA h g<sup>-1</sup>), which contains a large amount of polyanions relative to Fe, has a theoretical capacity 25% smaller than NASICON-type  $\text{Na}_2\text{Fe}_2(\text{SO}_4)_3$  (theoretical capacity: 134 mA h g<sup>-1</sup>). However, this disadvantage of eldfellite can be reversed by replacing Fe with V, which is capable of not only  $\text{M}^{2+}/\text{M}^{3+}$  but also the  $\text{M}^{3+}/\text{M}^{4+}$  redox. This is because eldfellite-type  $\text{Na}_x\text{V}(\text{SO}_4)_2$  has a theoretical capacity of 201 mA h g<sup>-1</sup> in the composition range of  $0 < x < 2$ , while NASICON-type  $\text{Na}_x\text{V}_2(\text{SO}_4)_3$  has only a theoretical capacity of 137 mA h g<sup>-1</sup> in the composition range of  $0 < x < 2$ .

For  $\text{NaV}(\text{SO}_4)_2$ , crystallographic studies and simple synthesis methods have already been reported.<sup>21–23</sup> High potentials of 2.42 and 4.61 V against  $\text{Na}/\text{Na}^+$  have been predicted for the  $\text{V}^{2+}/\text{V}^{3+}$  and  $\text{V}^{3+}/\text{V}^{4+}$  redoxes by DFT calculations by Banerjee *et al.*<sup>24</sup> However, to the best of our knowledge, no experimental studies on the electrochemical properties of  $\text{NaV}(\text{SO}_4)_2$  have yet been reported.

In the present study, eldfellite-type  $\text{NaV}(\text{SO}_4)_2$  was synthesized using a sol-gel method and the reversible capacity exceeding one electron reaction was confirmed in a wide voltage range between 1.5 and 4.8 V. The charge-discharge

<sup>a</sup> Interdisciplinary Graduate School of Engineering Sciences, Kyushu University, 6-1 Kasuga-koen, Kasuga, Fukuoka, 816-8580, Japan. E-mail: an40uvd@gmail.com, inoishi@cm.kyushu-u.ac.jp

<sup>b</sup> Institute for Materials Chemistry and Engineering, Kyushu University, 6-1 Kasuga-koen, Kasuga, Fukuoka, 816-8580, Japan

<sup>c</sup> Kyushu Synchrotron Light Research Center, 8-7 Yayoigaoka, Tosu, Saga, 841-0005, Japan

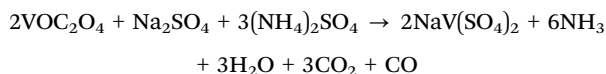
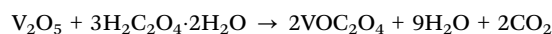
† Electronic supplementary information (ESI) available. See DOI: <https://doi.org/10.1039/d2ma00031h>

reaction mechanism was clarified through various *ex situ* measurements using X-rays in a laboratory or a synchrotron light facility, and these results were confirmed by computational calculations.

## Experimental

### Materials synthesis

NaV(SO<sub>4</sub>)<sub>2</sub> powder was synthesized according to the reported method.<sup>23</sup> H<sub>2</sub>C<sub>2</sub>O<sub>4</sub>·2H<sub>2</sub>O (FUJIFILM Wako; min 99.5–102.0%) and V<sub>2</sub>O<sub>5</sub> (Nacalai Tesque; min 99.0%) were mixed and agitated in ultrapure water at 80 °C for 1 h using a hotplate stirrer. The solution was initially orange and changed to green and then blue, indicating that V was reduced from the pentavalent to the tetravalent state. (NH<sub>4</sub>)<sub>2</sub>SO<sub>4</sub> (FUJIFILM Wako; min 99.5%) and Na<sub>2</sub>SO<sub>4</sub> (FUJIFILM Wako; min 99.0%) were then added, and the resultant aqueous solution was continuously stirred at 80 °C for 4 h. The solution was evaporated to dryness in an electric furnace at 120 °C for 12 h, resulting in a precursor powder. Finally, 0.8 g of the precursor powder was placed in an alumina crucible and heated in a tubular furnace at 375 °C (0.5 °C min<sup>−1</sup> heating rate) for 9 h under flowing Ar + 5% H<sub>2</sub> gas. Each reaction process in this synthesis, as previously reported,<sup>23</sup> is shown below:



### Materials characterization

The powder X-ray diffraction (XRD) patterns of NaV(SO<sub>4</sub>)<sub>2</sub> were recorded to identify its crystal structure at room temperature. The profiles were obtained using an X-ray diffractometer (TTRIII; Rigaku) equipped with a Cu Kα radiation source. The samples were measured in steps of 0.01° in the 2θ angular range from 10° to 130° at a scan rate of 0.1° min<sup>−1</sup>. An enclosed sample holder was used to exclude the effects of moisture in the air. The crystal structure was refined using the RIETAN-FP program,<sup>25</sup> and the crystal models were visualized using the VESTA software.<sup>26</sup> The sample morphology was observed by field-emission scanning electron microscopy (FE-SEM, JSM-IT700HR; JEOL).

### Electrochemical characterization

NaV(SO<sub>4</sub>)<sub>2</sub> and acetylene black (AB, Denka) were mixed in a ratio of 70:25 (by weight) using the ball-milling method (Premium line P-7; Fritsch) at 200 rpm for 3 h under an Ar atmosphere to increase the electronic conductivity of the electrode. The cathode was then prepared by blending the composite with a polytetrafluoroethylene (PTFE, Daikin) binder in a ratio of 95:5 (by weight) and then drying the electrode material at 80 °C under vacuum for 12 h. For electrochemical measurements, 2032 coin-type cells (Hohsen Co.) were washed ultrasonically with acetone and dried at 120 °C under vacuum before being transferred to a

glove box for cell assembly. Na metal (Sigma-Aldrich) was used as the counter and reference electrode. A polypropylene separator (Celgard) and a glass-fiber filter (GA-55; Advantec) were used as a separator in the cell. A 1 M NaPF<sub>6</sub> solution in ethylene carbonate (EC):diethyl carbonate (DEC) (1:1 by volume) (Tomiya Pure Chemical) or a 1 M NaClO<sub>4</sub> solution in EC:dimethyl carbonate (DMC) (1:1 by volume) (Tomiya Pure Chemical) was used as the electrolyte. All cathodes and cells were produced and assembled in an Ar-filled glove box (dew point < −80 °C). Electrochemical charge–discharge measurements were conducted *via* the galvanostatic method using a charge–discharge cycle instrument (BTS2400W; Nagano Electric Co.). The current density was 0.2 mA cm<sup>−2</sup>, and the galvanostatic measurements were conducted in a thermostat chamber at 25 °C.

### Ex situ X-ray measurements

*Ex situ* XRD measurements were performed to characterize the phase transitions during the charge–discharge processes. The XRD patterns were recorded at room temperature using an X-ray diffractometer (TTRIII; Rigaku) equipped with a Cu Kα radiation source. The measurements were performed in steps of 0.01° in the 2θ angular range from 10° to 40° at a scan rate of 0.02° min<sup>−1</sup>. The samples were obtained from coin cells disassembled in an Ar-filled glove box (dew point < −80 °C) after the electrochemical measurements and were dried under vacuum after being washed with DMC (Kishida Chemical) to remove the electrolyte on the pellet surface. An enclosed sample holder was used to exclude the effects of moisture in the air.

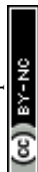
*Ex situ* X-ray photoelectron spectroscopy (XPS) measurements were conducted with Al Kα radiation using an ESCA 1600 (ULVAC-PHI) spectrometer. The samples were prepared in the same manner as those for *ex situ* XRD analysis. The obtained binding-energy data were corrected using the signal of adventitious carbon added to prevent charging up of the sample.

*Ex situ* X-ray absorption near-edge structure (XANES) measurements and *ex situ* near-edge X-ray absorption fine structure (NEXAFS) measurements were performed at the BL11 beamline (2100–23000 eV), BL12 beamline (40–1500 eV), and BL15 beamline (3500–23000 eV) of the Saga Light Source. Synchrotron radiation was used in the transmission mode (TM) for XANES measurements and the total fluorescence yield (TFY) mode for NEXAFS measurements at room temperature to determine the oxidation state of V during the charging and discharging processes. The samples were prepared using the same procedure described for the XPS samples, including washing with DMC. XANES data analysis was performed using the Athena software.<sup>27</sup>

For the XPS and NEXAFS measurements, a sample transfer vessel was used to avoid exposure to the air and to achieve a high-vacuum condition before the sample was introduced into the apparatus.<sup>28,29</sup>

### Computational calculations

First-principles calculations using density functional theory (DFT) were performed with the Vienna *Ab initio* Simulation Package (VASP).<sup>30,31</sup> The projector augmented-wave (PAW) method was used,<sup>32,33</sup> and the plane-wave cutoff energy was





set to 520 eV. The Perdew–Burke–Ernzerhof (PBE) exchange–correlation functional was applied.<sup>34</sup> The Hubbard  $U$  value for vanadium was set to 4.0 eV. The pymatgen package in Python was used for all DFT calculations to generate input files and analyze the results.<sup>35</sup> A unit cell ( $C2/m$ ) was used for the calculations, and a  $\Gamma$ -centered  $4 \times 4 \times 4$   $k$ -point mesh was used for the density of state (DOS) and electronic structure calculations. The 30 structures with the lowest electrostatic energies for each composition were subjected to the DFT calculations using the Supercell program,<sup>36</sup> and the most stable configuration was determined. The average voltage between each composition of  $\text{Na}_x\text{V}(\text{SO}_4)_2$  was obtained using the equation

$$V = -\frac{E(\text{Na}_{x_1}\text{V}(\text{SO}_4)_2) - E(\text{Na}_{x_2}\text{V}(\text{SO}_4)_2) - (x_1 - x_2)E(\text{Na})}{(x_1 - x_2)F}$$

where  $E(\text{Na}_{x_1}\text{V}(\text{SO}_4)_2)$ ,  $E(\text{Na}_{x_2}\text{V}(\text{SO}_4)_2)$ , and  $E(\text{Na})$  are DFT energies of  $\text{Na}_{x_1}\text{V}(\text{SO}_4)_2$ ,  $\text{Na}_{x_2}\text{V}(\text{SO}_4)_2$ , and Na metal, respectively. The Bader charge analysis was conducted on the basis of the calculation results of DOS using the Bader analysis program developed by Henkelman *et al.*<sup>37–39</sup>

## Results and discussion

### Computational calculations for $\text{Na}_x\text{V}(\text{SO}_4)_2$

The structural optimization was performed to evaluate the characteristics of  $\text{NaV}(\text{SO}_4)_2$  for each sodiated/desodiated composition. The first state formed a stable eldfellite structure with a monoclinic prismatic crystal class. Fig. 1a shows the formation energy convex hull construction of  $\text{Na}_x\text{V}(\text{SO}_4)_2$ . The formation energy of the composition  $x = 1.5$  is above the convex hull line, which means that this composition is unstable. Therefore, the compositions of  $x = 0, 0.5, 1$ , and  $2$  in  $\text{Na}_x\text{V}(\text{SO}_4)_2$  were adopted for further calculations and analyses. Fig. 1b shows the DFT-calculated average potential profiles of  $\text{Na}_x\text{V}(\text{SO}_4)_2$  ( $x = 0, 0.5, 1$ , and  $2$ ). Two potential plateaus are identified at  $\sim 2.2$  and  $\sim 4.6$  V, with two more-detailed potential plateaus at the higher potential of  $\sim 4.6$  V. Starting from the initial state of  $\text{NaV}(\text{SO}_4)_2$ , the theoretical capacities were estimated to be  $101 \text{ mA h g}^{-1}$  for a one-electron reaction and  $202 \text{ mA h g}^{-1}$  for a two-electron reaction. The results of the potential calculations show good agreement with previously reported results.<sup>24</sup> For the desodiation from  $\text{NaV}(\text{SO}_4)_2$ , we expected operation at a high potential such as  $\sim 4.7$  V vs.  $\text{Na}/\text{Na}^+$  using common electrolytes to be feasible because some materials have been reported to operate at higher potentials.<sup>40–42</sup>

### Materials characterization

$\text{NaV}(\text{SO}_4)_2$  was synthesized using the previously reported sol–gel method. We optimized the sintering time and temperature at 9 h and  $375^\circ\text{C}$  by attempting several sinter time/temperature combinations, although some small unknown impurities remained. The crystal structure of the synthesized  $\text{NaV}(\text{SO}_4)_2$  was determined by powder XRD *via* the Rietveld refinement using RIETAN-FP<sup>25</sup> (Fig. 2a). The results revealed that the compounds could be indexed to a monoclinic lattice of the space group  $C2/m$  and that

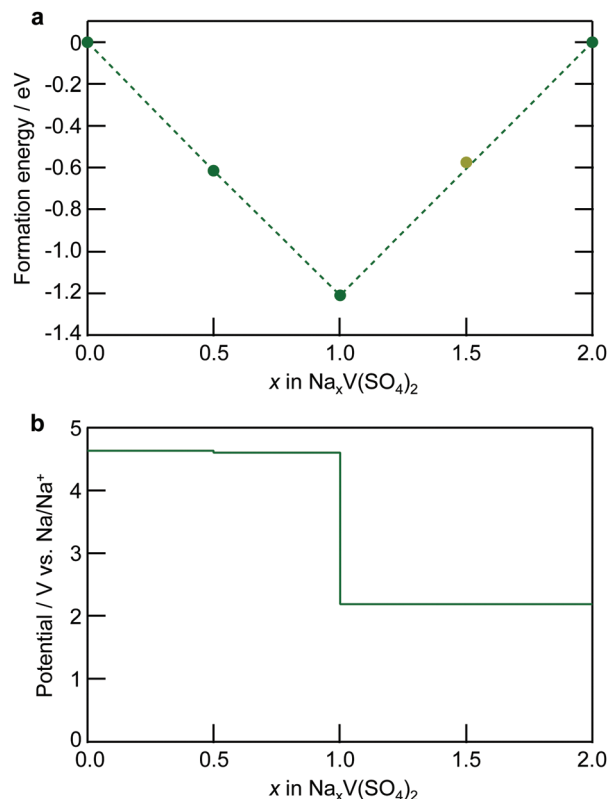


Fig. 1 (a) Formation energy convex hull construction and (b) potential profile for each composition of  $\text{Na}_x\text{V}(\text{SO}_4)_2$  ( $x = 0, 0.5, 1.0, 1.5$ , and  $2.0$ ).

the lattice parameters were  $a = 8.09(1)$ ,  $b = 5.180(6)$ ,  $c = 7.185(9)$ ,  $\beta = 92.067(7)^\circ$ , and  $V = 300.9(6) \text{ \AA}^3$ , which is larger than the unit-cell volume of  $\text{NaFe}(\text{SO}_4)_2$ <sup>13</sup> because of the larger ionic radius of  $\text{V}^{3+}$  ( $0.640 \text{ \AA}$ ) compared with that of  $\text{Fe}^{3+}$  ( $0.61 \text{ \AA}$ ) in a hexagonal system. These parameters are consistent with the previous research on the synthesis of  $\text{NaV}(\text{SO}_4)_2$ .<sup>23</sup> The Rietveld-refined parameters were satisfactory, with  $R_{\text{wp}} = 6.16\%$ ,  $R_p = 4.63\%$ , and  $S = 1.29$ . However,  $\sim 3 \text{ wt\%}$  of  $\text{V}_2\text{O}_3(\text{SO}_4)_2$  was confirmed as a sub-phase material; this material has been reported to be lithiated between 1.95 and 4.20 V.<sup>43</sup> The crystal structure was obtained from the Rietveld refinement results (Fig. 2b). Na ions were connected to the  $\text{VO}_6$  octahedra and  $\text{SO}_4$  tetrahedra *via* six surrounding oxygen atoms. The morphologies of the as-prepared  $\text{NaV}(\text{SO}_4)_2$  powder were confirmed by SEM observation (Fig. 2c and d). The powder exhibited a moisture-absorbent character as shown in Fig. S1 (ESI†); the samples were therefore carefully transported to the measuring equipment without exposure to moisture in the air. The particle shape and grain size were dramatically changed and refined by ball milling.

### Electrochemical properties

The galvanostatic properties of the composite electrode, including  $\text{NaV}(\text{SO}_4)_2$  as the active material, are shown in Fig. 3. The measurement voltage ranges were found to be 1.5–3.2 V (vs.  $\text{Na}/\text{Na}^+$ ) for the sodiation/desodiation process ( $1 \leq x \leq 2$  in  $\text{Na}_x\text{V}(\text{SO}_4)_2$ ) from the initial state of  $\text{NaV}(\text{SO}_4)_2$  and 3.2–4.8 V with a theoretical capacity limitation of  $101 \text{ mA h g}^{-1}$  for the desodiation/sodiation process



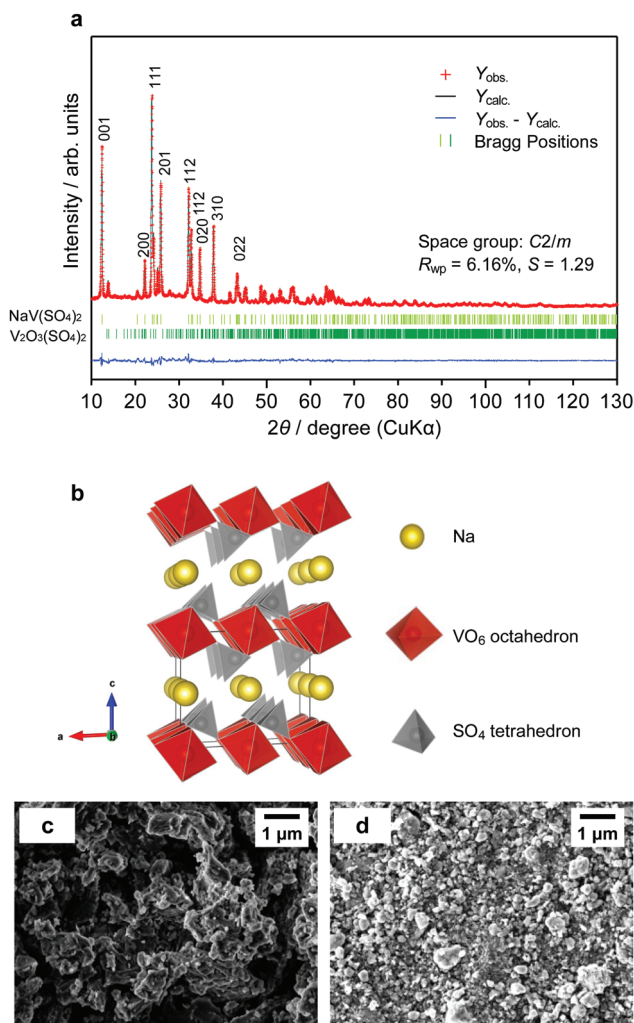


Fig. 2 (a) XRD pattern and the results of the Rietveld refinement of the as-prepared  $\text{NaV}(\text{SO}_4)_2$ . (b) The crystal structure obtained from the Rietveld-refined  $\text{NaV}(\text{SO}_4)_2$ . The structure was visualized using VESTA. SEM images of the (c) as-prepared  $\text{NaV}(\text{SO}_4)_2$  and (d) carbon-coated  $\text{NaV}(\text{SO}_4)_2$  prepared by ball milling.

( $0 \leq x \leq 1$  in  $\text{Na}_x\text{V}(\text{SO}_4)_2$ ). For the sodiation/desodiation process in Fig. 3a, a potential plateau was observed at 2.3 V (vs.  $\text{Na}/\text{Na}^+$ ). From the reversible capacity and potential values, the average working potential was calculated to be 2.1 V, which is consistent with the average potential calculated by DFT. This value is the highest potential reported for the  $\text{V}^{2+}/\text{V}^{3+}$  redox couple in any material because of the greater inductive effect of  $\text{SO}_4^{2-}$  compared with that of other counter anions. The reversible capacity in the first cycle was  $77 \text{ mA h g}^{-1}$ , which is greater than 75% of the theoretical capacity. After the second cycle,  $\text{NaV}(\text{SO}_4)_2$  showed good cyclability, with better than 95% coulombic efficiency, and the capacity retention was 60% in the 30th cycle. The discharge-charge capacities of  $\text{NaV}(\text{SO}_4)_2$  are comparable to those of  $\text{NaFe}(\text{SO}_4)_2$  ( $\text{Fe}^{2+}/\text{Fe}^{3+}$ ).<sup>13</sup> The potential difference of 1 V between  $\text{NaV}(\text{SO}_4)_2$  and  $\text{NaFe}(\text{SO}_4)_2$  was reasonably attributed to the typical potential gap between  $\text{V}^{2+}/\text{V}^{3+}$  and  $\text{Fe}^{2+}/\text{Fe}^{3+}$ , similar to the difference observed between the NASICON-type materials  $\text{Na}_3\text{V}_2(\text{PO}_4)_3$  (1.5 or 1.6 V) and

$\text{Na}_3\text{Fe}_2(\text{PO}_4)_3$  (2.5 V).<sup>18–20,44–46</sup> Different electrolyte types did not affect the discharge-charge properties in the sodiation/desodiation process from the initial state of  $\text{NaV}(\text{SO}_4)_2$ , as shown in Fig. 3a and c.

However, in terms of the desodiation/sodiation process from the initial composition, different electrolyte types resulted in different galvanostatic charge-discharge profiles. Fig. 3b and d shows the charge-discharge profiles for the two electrolytes. For the  $\text{NaPF}_6$ -type electrolyte as shown in Fig. S2 (ESI<sup>†</sup>), the potential of the  $\text{NaV}(\text{SO}_4)_2$  cell decreased and remained  $\sim 3.7$  V; in addition, the cell charged beyond its theoretical capacity based on the one-electron reaction in  $\text{NaV}(\text{SO}_4)_2$  after reaching 4.1 V at a charging capacity of  $19 \text{ mA h g}^{-1}$ . By contrast, for the  $\text{NaClO}_4$ -based electrolyte as shown in Fig. 3d, no potential decrease was observed even after the highest potential was reached in the charging process. These charging profiles likely indicate electrolyte decomposition even though the literature includes few examples of redox reactions that operate at equal or higher potentials than those in the present study.<sup>40,41</sup> Therefore, the capacity was regulated at  $101 \text{ mA h g}^{-1}$  for this process to force this decomposition reaction to stop at the one-electron theoretical capacity of  $\text{NaV}(\text{SO}_4)_2$ . A small reversible capacity of  $2 \text{ mA h g}^{-1}$  was observed in the cell with 1 M  $\text{NaPF}_6$  in EC:DEC (1:1 by volume), whereas a reversible capacity of  $25 \text{ mA h g}^{-1}$  was obtained with an average working potential of 3.9 V in the cell with 1 M  $\text{NaClO}_4$  in EC:DMC (1:1 by volume) at the first cycle. In the second cycle, for the  $\text{NaClO}_4$ -type electrolyte, the reversible capacity increased to  $31 \text{ mA h g}^{-1}$ , which is 30% of the one-electron theoretical capacity of  $\text{NaV}(\text{SO}_4)_2$ , and then gradually decreased from the third cycle. Here, the types of solvent in the electrolytes did not significantly affect the voltage profiles while the cycling performance was slightly improved by using 1 M  $\text{NaClO}_4$  in EC:DMC:FEC (49:49:2 by volume) as the electrolyte (Fig. S3 and S4, ESI<sup>†</sup>). Oxidative decomposition of the electrolyte is unavoidable in this material during charge-discharge operations at high potentials, resulting in lower capacities and working potentials than those calculated.  $\text{NaV}(\text{SO}_4)_2$  was found to be reversibly charged and discharged, at least in the  $\text{NaClO}_4$ -based electrolyte. However, the longer the rest time after charging, the more the discharge capacity decreased according to Fig. S5 (ESI<sup>†</sup>). Thus, even in the  $\text{NaClO}_4$ -based electrolyte, the progression of the side reactions or electrolyte decomposition caused by holding the electrolyte at high potentials cannot be suppressed. If the oxidative decomposition of the electrolyte can be prevented at high voltages, the working potential and reversible capacity should increase further because the capacity corresponding to the sloped part of the charging curve coincides with that corresponding to the discharging curve.

A charge-discharge diagram corresponding to a broader potential range (1.5–4.8 V) is shown in Fig. 3e. The charging capacity was found to be  $101 \text{ mA h g}^{-1}$  from the open-circuit potential at the first cycle; from the second cycle onward, the charging capacity was also found to be  $101 \text{ mA h g}^{-1}$  after charging from 1.5 V to 3.2 V. Both the charge and discharge capacities exceeded  $101 \text{ mA h g}^{-1}$ , and the discharge capacity



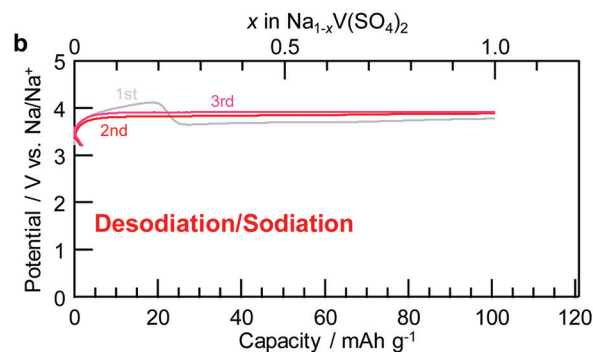
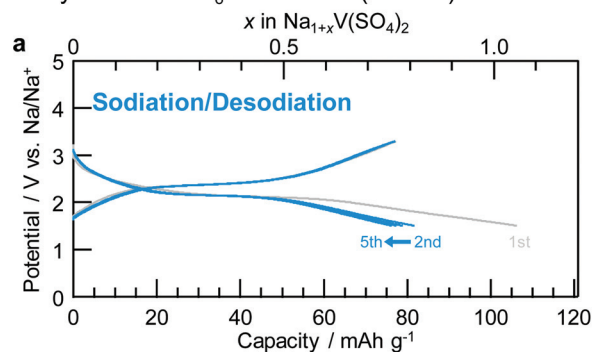
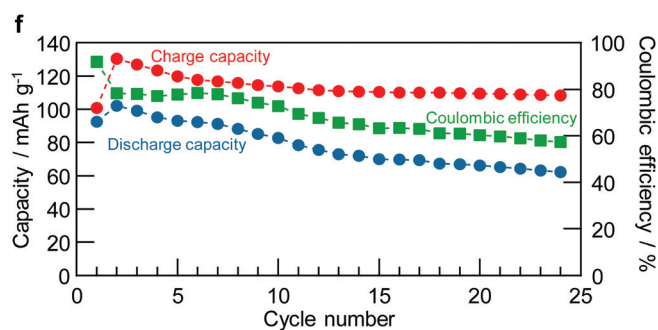
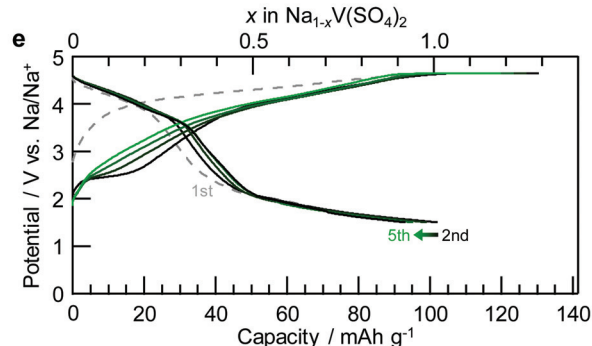
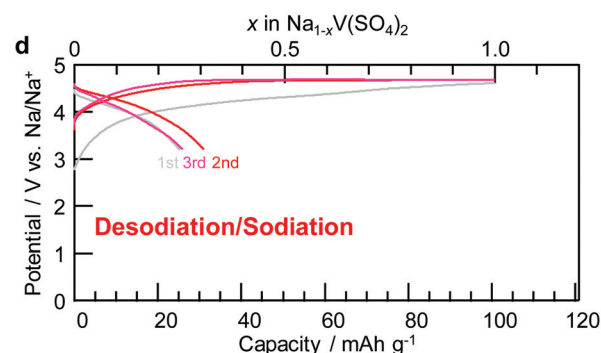
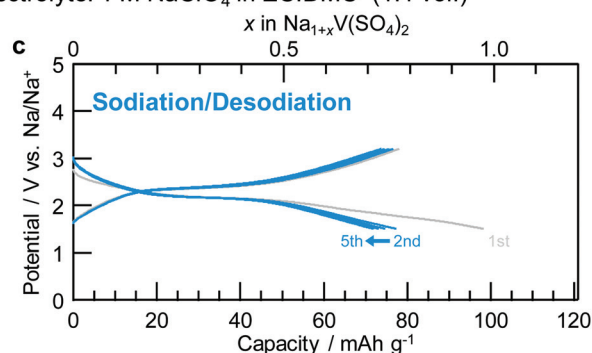
Electrolyte: 1 M NaPF<sub>6</sub> in EC:DEC (1:1 vol.)Electrolyte: 1 M NaClO<sub>4</sub> in EC:DMC (1:1 vol.)

Fig. 3 Charge–discharge profiles of NaV(SO<sub>4</sub>)<sub>2</sub> showing sodiation and desodiation in cells prepared with two different electrolytes: (a) and (b) 1 M NaPF<sub>6</sub> in EC : DEC (1 : 1 by volume) and (c) and (d) 1 M NaClO<sub>4</sub> in EC : DMC (1 : 1 by volume). (e) Charge–discharge profiles and (f) cycle performance of NaV(SO<sub>4</sub>)<sub>2</sub> in the voltage region of 1.5–4.8 V; the electrolyte was 1 M NaClO<sub>4</sub> in EC : DMC (1 : 1 by volume).

reached 102 mA h g<sup>−1</sup> for the second cycle. Fig. S6 (ESI†) shows the dQ/dV curves obtained from the initial charge–discharge measurement. Two steps of the redox peak could be identified, although the decomposition of the electrolyte at high potentials made it difficult to distinguish the oxidation peak. As demonstrated in Fig. 3f, the decrease in the charge capacity with each cycle mostly stopped at a certain level; however, the discharge capacity and coulombic efficiency decreased with each cycle, likely because of the electrolysis of the electrolyte caused by repeated cycling at high potentials.

### Crystal structure analysis

Fig. 4 shows the *ex situ* XRD patterns during the charge–discharge process for the first cycle. The states of charge during the sodiation/desodiation or desodiation/sodiation process are indicated in the charge–discharge profiles next to the XRD

profiles. All the patterns were applied without any corrections because Soller slits were installed for the parallel-beam method for the XRD measurements as a consequence of the peak of PTFE appearing at the same angle (18°) for all the samples. For the sodiation/desodiation process (blue and sky-blue lines), peak shifts to lower angles were observed from the initial state to the 1.5 V discharged state, and the peaks were recovered to the original position by 3.2 V charging at 12.3°, 23.7°, 25.8°, and 32.1°, which were assigned as the (001), (111̄), (201), and (112̄) Bragg peaks, respectively. The shift to smaller angles indicates that the insertion of Na<sup>+</sup> led to an increase in the lattice parameter. In addition, the peak intensity ratios for the peak groups at ~12°, ~25°, and ~32.5° were reversibly changed. Therefore, they tended to be comparable to the simulated XRD patterns visualized by VESTA<sup>26</sup> on the basis of the DFT calculations (Fig. S7, ESI†). Moreover, two new peaks appeared at 22.6°



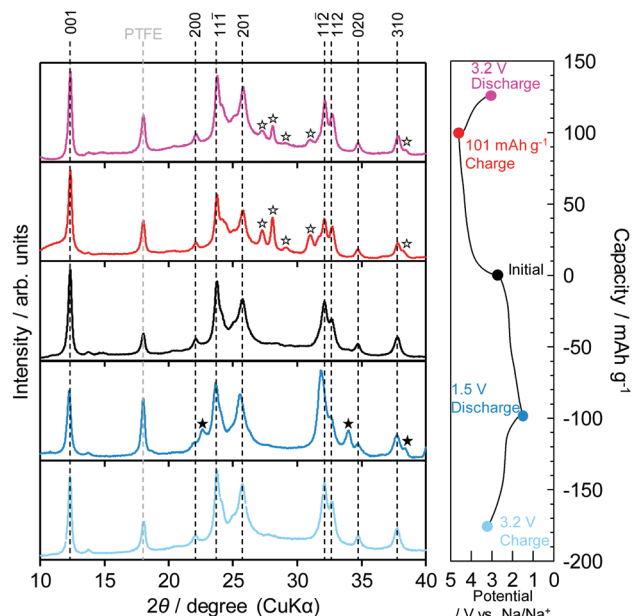


Fig. 4 *Ex situ* XRD patterns during galvanostatic measurements using 1 M NaClO<sub>4</sub> in EC : DMC (1 : 1 by volume) as the electrolyte for the initial state (black line), the desodiation/sodiation process (red and pink lines), and the sodiation/desodiation process (blue and light-blue lines). Black and white star icons show the new diffraction peaks on the discharging and charging process, respectively.

and 34° (pointed out by black stars), indicating a two-phase mechanism after discharge to 1.5 V; these peaks fully recovered after charging to 3.2 V.

Similarly, for the desodiation/sodiation process lined in red and pink, the intensity ratios between the peak groups of 12° and 25° were reversibly changed: the peak group at ~12°

increased after 101 mA h g<sup>-1</sup> charging and then recovered to the initial state after discharge to 3.2 V. New peaks were also observed at ~27.5° and ~31.2° (pointed out by white stars) after desodiation by charging to 101 mA h g<sup>-1</sup>; the intensities of these peaks then decreased upon sodiation by discharging to 3.2 V, but the initial patterns were not fully recovered. These results confirm that single-phase and two-phase reactions occur during both the sodiation/desodiation and desodiation/sodiation processes from the initial composition.

### Oxidation-state analysis

Oxidation-state analysis was conducted to investigate the redox center of NaV(SO<sub>4</sub>)<sub>2</sub> during the charge–discharge process by *ex situ* XANES measurements using hard X-rays and *ex situ* NEXAFS measurements using soft X-rays. Here, we used two different beamlines for soft (40–1500 eV) and hard (2100–23000 eV) X-rays to cover the targeted energy range. The V K-edge XANES spectra were recorded in the hard X-ray range to determine the oxidation state of V during the charge–discharge measurements (Fig. 5b and c). Each state of charge was found to match the charge–discharge profiles in Fig. 5a. In the sodiation/desodiation process from the initial state (Fig. 5b), the K-edge of V shifted to lower energy upon discharge to 1.5 V and shifted to higher energy and returned to the initial position upon charging to 3.2 V. These results indicate that a reversible V redox reaction occurred. Compared with the standard samples of vanadium oxides of VO (V<sup>2+</sup>) and V<sub>2</sub>O<sub>3</sub> (V<sup>3+</sup>) in Fig. S8 (ESI<sup>†</sup>), the initial oxidation state of V<sup>3+</sup> changes to V<sup>2+</sup> upon sodiation and then returns to the original V<sup>3+</sup> upon desodiation. However, during the desodiation/sodiation process from the initial state, the shift at the absorption edge was negligible (Fig. 5c). However, the second-derivative profiles of the adsorption edge imply a minor shift toward higher energy by

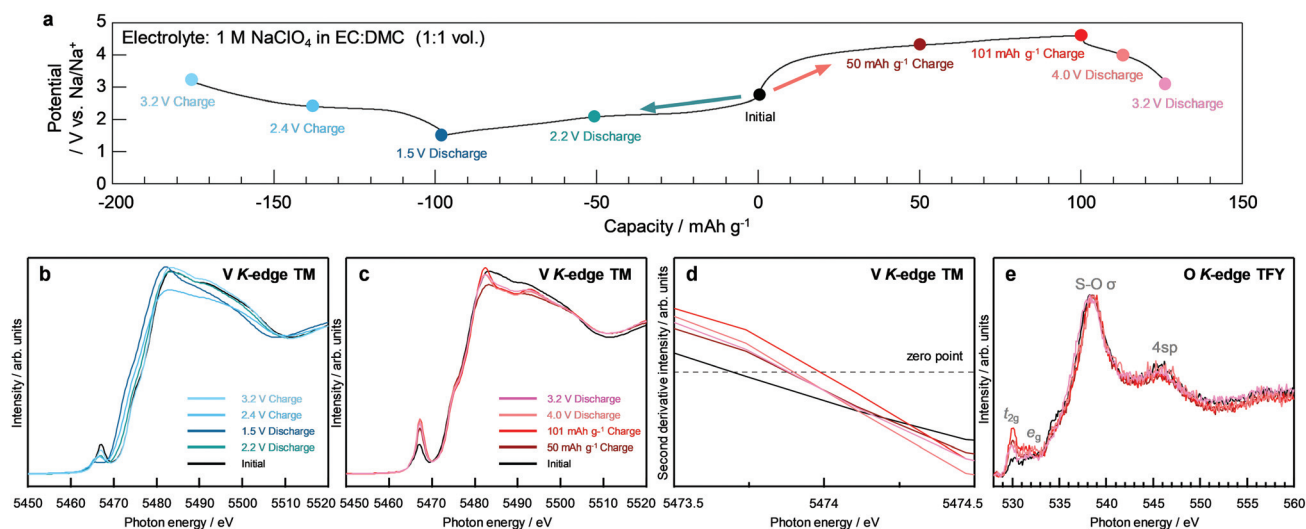


Fig. 5 (a) Charge–discharge profiles of NaV(SO<sub>4</sub>)<sub>2</sub>, showing the state of charge when 1 M NaClO<sub>4</sub> EC : DMC (1 : 1 by volume) was used. V K-edge XANES spectra of NaV(SO<sub>4</sub>)<sub>2</sub> at the different charge–discharge states during the first cycle for the (b) sodiation/desodiation process and (c) desodiation/sodiation process from the initial composition. (d) Second-derivative profiles during the desodiation/sodiation process to check the shift of the inflection point at the absorption edge. Transmission mode (TM) was used for the XANES measurements. (e) O K-edge NEXAFS spectra of NaV(SO<sub>4</sub>)<sub>2</sub> at different charge–discharge states during the first cycle for the desodiation/sodiation process from the initial composition. The TFY mode was used for the NEXAFS measurements.

desodiation and toward lower energy upon sodiation (Fig. 5d). Moreover, from the pre-edge region at  $\sim 5467$  eV, which represents the forbidden transition from the 1s to 3d orbitals, the peak increased upon charging and decreased upon discharging, indicating the introduction and disappearance of a hole in the electronic state of V in the 3d orbitals. When 1 M NaPF<sub>6</sub> in EC:DEC (1:1 by volume) was used (Fig. S8, ESI†), none of the spectra changed during the desodiation/sodiation process, indicating that no reaction occurred during charging/discharging, although a similar valence change was observed in the sodiation/desodiation process.

The *ex situ* NEXAFS measurements using soft X-rays reveal that the oxidation states of O also changed at the respective states of charge (Fig. 5e). The photon energy values in the NEXAFS spectra were corrected on the basis of the binding energy of the adventitious carbon in another synchrotron XPS measurement. Fig. 5e shows the O K-edge TFY spectrum. The spectral features that originate from O 2p orbitals hybridized with surrounding elements are well known to reflect the electronic states around oxide ions.<sup>41,47–49</sup> The NEXAFS O K-edge spectra of NaV(SO<sub>4</sub>)<sub>2</sub> were likely constructed from the O 2p orbitals hybridized with V 3d (*t*<sub>2g</sub> and/or *e*<sub>g</sub>) and V 4sp, and S–O  $\sigma$ -bond signals appeared at approximately 529.6, 531.6, 545, and 538 eV.<sup>49</sup> The peak at 529.6 eV corresponds to the unoccupied hybridized orbital of the O 2p orbital and V 3d (*t*<sub>2g</sub>) orbital,<sup>49–51</sup> and this peak partially reversibly changed during the desodiation/sodiation process (*i.e.*, increasing in the intensity during desodiation and decreasing during sodiation). Meanwhile, the spectra at 538 and 545 eV did not change, and the corresponding hybridized orbitals, which were S–O  $\sigma$ -bonding and O 2p–V 4sp, respectively, did not play a prominent role in the charge-transfer mechanism. These XANES and NEXAFS measurements imply the charge compensation of V and O during the desodiation/sodiation process in NaV(SO<sub>4</sub>)<sub>2</sub>. The *ex situ* XPS measurements dynamically revealed the redox reaction of V and O (Fig. S9, ESI†). Given the difference in the depth of detection for each measurement (*i.e.*, through the entire sample in the case of XANES-TM, several hundred nanometers to one micrometer in the case of NEXAFS-TFY, and several nanometers in the case of XPS), the redox reaction can be assumed to have proceeded best near the electrode surface.

The DFT calculations for the electronic structure support the assigned oxidation state of each element, as demonstrated in Fig. 6 for the projected density of states (pDOS) diagrams. The overall diagrams of the pDOS are shown in Fig. S10 (ESI†). The pDOS in Na<sub>x</sub>V(SO<sub>4</sub>)<sub>2</sub> reveals that NaV(SO<sub>4</sub>)<sub>2</sub> holds the V 3d and O 2p hybridization state just below the Fermi level and that the V–O hybridized bands emerge above the bandgap upon desodiation. Notably, the S bands were configured at the deep level and the S element did not play roles in the charge compensation (Fig. S10, ESI†). In addition, the Bader charge analysis (Fig. 7; the raw values are shown in Table S2, ESI†) undoubtedly suggests that charge transfer occurred at the V–O hybridized orbitals. The Bader charges increased with the decreasing amount of Na ions in Na<sub>x</sub>V(SO<sub>4</sub>)<sub>2</sub>, and the charge compensation by V and O was assumed, whereas V mainly

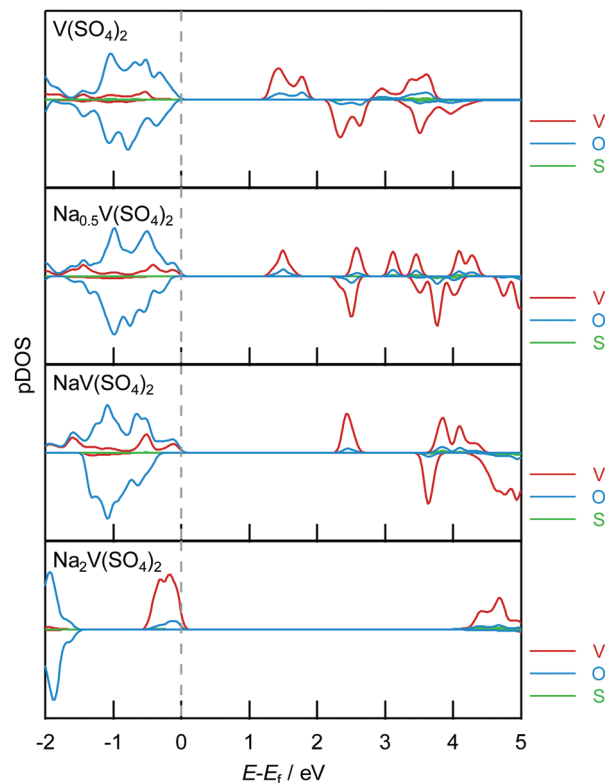


Fig. 6 Calculated partial density of states (pDOS) of Na<sub>x</sub>V(SO<sub>4</sub>)<sub>2</sub> ( $x = 0, 0.5, 1$ , and  $2$ ), as obtained using DFT calculations. The dashed line is the Fermi energy level.

compensated for the charge transfer in the sodiation process from NaV(SO<sub>4</sub>)<sub>2</sub> to Na<sub>2</sub>V(SO<sub>4</sub>)<sub>2</sub>. In addition, the magnetic moments (Table S2, ESI†) enable us to estimate the electron configurations of the ions, and the oxidation states of the redox-centric element can therefore be assumed for compositions with various Na contents.<sup>52</sup> In NaV(SO<sub>4</sub>)<sub>2</sub>, the magnetic moment on V is 1.912, corresponding to a d-electron configuration of d<sup>2</sup>. Upon desodiation, the magnetic moments on both V and O decreased, indicating the oxidation of V and O ions even though the decrease

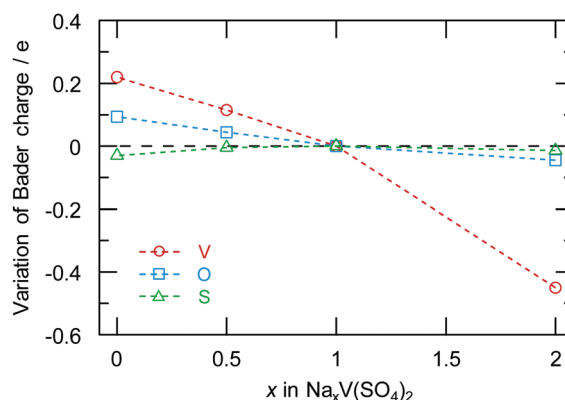


Fig. 7 Variation of the Bader charge for V, O, and S in Na<sub>x</sub>V(SO<sub>4</sub>)<sub>2</sub> ( $x = 0, 0.5, 1, 2$ ), as obtained using DFT calculations. The Bader charges were normalized on the basis of the Bader charge of NaV(SO<sub>4</sub>)<sub>2</sub>. The raw data for the Bader charges for O and V are shown in Table S2 (ESI†).





in the magnetic moment in O was not dramatic. These NEXAFS spectral changes and DFT calculation results indicate that charge transfer occurred during the desodiation/sodiation process and provide evidence for the charge compensation of V 3d and O 2p.

## Conclusions

Eldfellite-type  $\text{NaV}(\text{SO}_4)_2$  was investigated *via* experimental measurements and computational calculations. First-principles calculations predicted  $\text{Na}_x\text{V}(\text{SO}_4)_2$  to act at average potentials of 2.2 and 4.6 V for the process of  $\text{Na}_2\text{V}(\text{SO}_4)_2 \rightarrow \text{NaV}(\text{SO}_4)_2 \rightarrow \text{V}(\text{SO}_4)_2$ .  $\text{NaV}(\text{SO}_4)_2$  electrochemically delivered maximum reversible capacities of 77 and 31 mA h g<sup>-1</sup> with working potentials of 2.1 and 3.9 V for the sodiation/desodiation and desodiation/sodiation processes, respectively. By enlarging the regulation potential to employ a two-step redox reaction, we obtained a maximum discharge capacity of 102 mA h g<sup>-1</sup>. The energy density of 266 W h kg<sup>-1</sup> is less than that of other polyanionic cathode materials, but, in consideration of the theoretical value (708 W h kg<sup>-1</sup>),  $\text{NaV}(\text{SO}_4)_2$  may target very excellent properties by improving the electrolyte (Fig. S11, ESI†). *Ex situ* XRD measurements revealed phase transitions, including a reversible expansion/contraction or a transformation to an unknown phase, during the charge-discharge process. The charge compensation in the charge-discharge process was carried out by V in sodiation/desodiation and by strong V and small O contributions in desodiation/sodiation. This mechanism was supported by the variation of the pDOS and the Bader charges for  $\text{Na}_x\text{V}(\text{SO}_4)_2$ .

## Author contributions

Akira Nishio: conceptualization, formal analysis, investigation, methodology, validation, and writing – original draft preparation. Yuji Ishado: software. Kosuke Nakamoto: investigation. Eiichi Kobayashi: formal analysis and investigation. Atsushi Inoishi: conceptualization, funding acquisition, investigation, methodology, and supervision. Hikari Sakaabe: methodology. Shigeto Okada: funding acquisition and supervision. All the authors contributed to writing – review and editing, and approved the final report. The author contributions were noted using CRediT.

## Conflicts of interest

There are no conflicts to declare.

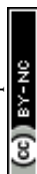
## Acknowledgements

This work was financially supported by the MEXT, Japan (ESICB program (JPMXP0112101003) and “Five-star Alliance”) and the JSPS (KAKENHI Grant no. JP20H05297). The experiments using synchrotron radiation were performed at beamlines BL11, BL12, and BL15 of the SAGA Light Source (Proposal No. 1911107R, 2006052R/BL11, 2007070R, 2102009A/BL12, and 2109085R/BL15). DFT calculations were carried out using the

computer resources offered under the category of General Projects by the Research Institute for Information Technology, Kyushu University.

## References

- 1 C. Masquelier and L. Croguennec, *Chem. Rev.*, 2013, **113**, 6552–6591.
- 2 P. Barpanda, L. Lander, S. I. Nishimura and A. Yamada, *Adv. Energy Mater.*, 2018, **8**, 1703055.
- 3 T. Jin, H. Li, K. Zhu, P. F. Wang, P. Liu and L. Jiao, *Chem. Soc. Rev.*, 2020, **49**, 2342–2377.
- 4 S. K. Sapra, J. Pati, P. K. Dwivedi, S. Basu, J. Chang and R. S. Dhaka, *WIREs Energy Environ.*, 2021, **10**, 37.
- 5 A. Manthiram and J. B. Goodenough, *J. Solid State Chem.*, 1987, **71**, 349–360.
- 6 A. Manthiram and J. B. Goodenough, *J. Power Sources*, 1989, **26**, 403–408.
- 7 K. S. Nanjundaswamy, A. K. Padhi, J. B. Goodenough, S. Okada, H. Ohtsuka, H. Arai and J. Yamaki, *Solid State Ionics*, 1996, **92**, 1–10.
- 8 S. Okada, H. Arai and J. Yamaki, *Denki Kagaku*, 1997, **65**, 802–808.
- 9 D. Dwivedi and P. Barpanda, *Mater. Today: Proc.*, 2018, **5**, 23439–23442.
- 10 W. Pan, W. Guan, S. Liu, B. Bin Xu, C. Liang, H. Pan, M. Yan and Y. Jiang, *J. Mater. Chem. A*, 2019, **7**, 13197–13204.
- 11 P. Barpanda, J. N. Chotard, N. Recham, C. Delacourt, M. Ati, L. Dupont, M. Armand and J. M. Tarascon, *Inorg. Chem.*, 2010, **49**, 7401–7413.
- 12 R. Tripathi, T. N. Ramesh, B. L. Ellis and L. F. Nazar, *Angew. Chem., Int. Ed.*, 2010, **49**, 8738–8742.
- 13 P. Singh, K. Shiva, H. Celio and J. B. Goodenough, *Energy Environ. Sci.*, 2015, **8**, 3000–3005.
- 14 P. Barpanda, G. Oyama, C. D. Ling and A. Yamada, *Chem. Mater.*, 2014, **26**, 1297–1299.
- 15 S. C. Chung, J. Ming, L. Lander, J. Lu and A. Yamada, *J. Mater. Chem. A*, 2018, **6**, 3919–3925.
- 16 C. W. Mason, I. Gocheva, H. E. Hoster and D. Y. W. Yu, *Chem. Commun.*, 2014, **50**, 2249–2251.
- 17 A. Kitajou, H. Momida, T. Yamashita, T. Oguchi and S. Okada, *ACS Appl. Energy Mater.*, 2019, **2**, 5968–5974.
- 18 Y. Uebou, T. Kiyabu, S. Okada and J. Yamaki, *Rep. Inst. Adv. Mater. Study, Kyushu Univ.*, 2002, **16**, 1–5.
- 19 R. Rajagopalan, B. Chen, Z. Zhang, X. L. Wu, Y. Du, Y. Huang, B. Li, Y. Zong, J. Wang, G. H. Nam, M. Sindoro, S. X. Dou, H. K. Liu and H. Zhang, *Adv. Mater.*, 2017, **29**, 1605694.
- 20 Y. Liu, Y. Zhou, J. Zhang, Y. Xia, T. Chen and S. Zhang, *ACS Sustainable Chem. Eng.*, 2017, **5**, 1306–1314.
- 21 R. Fehrmann, S. Boghosian, G. N. Papatheodorou, K. Nielsen, R. W. Berg, N. J. Bjerrum and A. E. Underhill, *Acta Chem. Scand.*, 1991, **45**, 961–964.
- 22 S. Boghosian, R. Fehrmann, K. Nielsen, G. Liptay, R. Snoeck, J. Balzarini, B. Fransson, U. Ragnarsson and G. W. Francis, *Acta Chem. Scand.*, 1994, **48**, 724–731.



- 23 L. L. Driscoll, A. J. Wright and P. R. Slater, *Dalton Trans.*, 2018, **47**, 13535–13542.
- 24 A. Banerjee, R. B. Araujo and R. Ahuja, *J. Mater. Chem. A*, 2016, **4**, 17960–17969.
- 25 F. Izumi and K. Momma, *Solid State Phenom.*, 2007, **130**, 15–20.
- 26 K. Momma and F. Izumi, *J. Appl. Crystallogr.*, 2011, **44**, 1272–1276.
- 27 B. Ravel and M. Newville, *J. Synchrotron Radiat.*, 2005, **12**, 537–541.
- 28 E. Kobayashi, J. Meikaku, H. Setoyama and T. Okajima, *J. Surf. Anal.*, 2012, **19**, 2–5.
- 29 E. Kobayashi, D. Yoshimura, H. Setoyama and T. Okajima, *J. Vac. Soc. Jpn.*, 2016, **59**, 341–345.
- 30 G. Kresse and J. Furthmüller, *Comput. Mater. Sci.*, 1996, **6**, 15–50.
- 31 G. Kresse and J. Furthmüller, *Phys. Rev. B: Condens. Matter Mater. Phys.*, 1996, **54**, 11169–11186.
- 32 P. E. Blöchl, *Phys. Rev. B: Condens. Matter Mater. Phys.*, 1994, **50**, 17953–17979.
- 33 D. Joubert, *Phys. Rev. B: Condens. Matter Mater. Phys.*, 1999, **59**, 1758–1775.
- 34 J. P. Perdew, K. Burke and M. Ernzerhof, *Phys. Rev. Lett.*, 1996, **77**, 3865–3868.
- 35 S. P. Ong, W. D. Richards, A. Jain, G. Hautier, M. Kocher, S. Cholia, D. Gunter, V. L. Chevrier, K. A. Persson and G. Ceder, *Comput. Mater. Sci.*, 2013, **68**, 314–319.
- 36 K. Okhotnikov, T. Charpentier and S. Cadars, *J. Cheminf.*, 2016, **8**, 17.
- 37 G. Henkelman, A. Arnaldsson and H. Jónsson, *Comput. Mater. Sci.*, 2006, **36**, 354–360.
- 38 W. Tang, E. Sanville and G. Henkelman, *J. Phys.: Condens. Matter*, 2009, **21**, 084204.
- 39 M. Yu and D. R. Trinkle, *J. Chem. Phys.*, 2011, **134**, 064111.
- 40 K. Kawai, W. Zhao, S. Nishimura and A. Yamada, *ACS Appl. Energy Mater.*, 2018, **1**, 928–931.
- 41 K. Kawai, D. Asakura, S. I. Nishimura and A. Yamada, *Chem. Mater.*, 2021, **33**, 1373–1379.
- 42 M. Sun, G. Rousse, M. Saubanière, M. L. Doublet, D. Dalla Corte and J. M. Tarascon, *Chem. Mater.*, 2016, **28**, 6637–6643.
- 43 S. F. Linnell, J. L. Payne, D. M. Pickup, A. V. Chadwick, A. R. Armstrong and J. T. S. Irvine, *J. Mater. Chem. A*, 2020, **8**, 19502–19512.
- 44 Y. Ishado, A. Inoishi and S. Okada, *Electrochemistry*, 2020, **88**, 457–462.
- 45 Q. Wang, J. Xu, W. Zhang, M. Mao, Z. Wei, L. Wang, C. Cui, Y. Zhu and J. Ma, *J. Mater. Chem. A*, 2018, **6**, 8815–8838.
- 46 J. N. Chotard, G. Rousse, R. David, O. Mentré, M. Courty and C. Masquelier, *Chem. Mater.*, 2015, **27**, 5982–5987.
- 47 D. Asakura, E. Hosono, M. Okubo, Y. Nanba, H. Zhou, P. A. Glans and J. Guo, *Chem. Phys. Chem.*, 2016, **17**, 4110–4115.
- 48 D. Asakura, Y. Nanba, Y. Makinose, H. Matsuda, P. A. Glans, J. Guo and E. Hosono, *Chem. Phys. Chem.*, 2018, **19**, 988–992.
- 49 C. J. Patridge, C. Jaye, T. A. Abtew, B. Ravel, D. A. Fischer, A. C. Marschilok, P. Zhang, K. J. Takeuchi, E. S. Takeuchi and S. Banerjee, *J. Phys. Chem. C*, 2011, **115**, 14437–14447.
- 50 M. Abbate, H. Pen, M. T. Czyzyk, F. M. F. de Groot, J. C. Fuggle, Y. J. Ma, C. T. Chen, F. Sette, A. Fujimori, Y. Ueda and K. Kosuge, *J. Electron Spectrosc. Relat. Phenom.*, 1993, **62**, 185–195.
- 51 Y. Kim, G. Y. Song, R. Nandi, J. Y. Cho, J. Heo and D. Y. Cho, *RSC Adv.*, 2020, **10**, 26588–26593.
- 52 H. Gao, I. D. Seymour, S. Xin, L. Xue, G. Henkelman and J. B. Goodenough, *J. Am. Chem. Soc.*, 2018, **140**, 18192–18199.

